

A Systematic Relationship between Intraseasonal Variability and Mean State Bias in AGCM Simulations

DAEHYUN KIM

Lamont-Doherty Earth Observatory, Columbia University, Palisades, New York

ADAM H. SOBEL

Department of Applied Physics and Applied Mathematics, and Department of Earth and Environmental Sciences, Columbia University, New York, New York

ERIC D. MALONEY

Department of Atmospheric Science, Colorado State University, Fort Collins, Colorado

DARGAN M. W. FRIERSON

Department of Atmospheric Sciences, University of Washington, Seattle, Washington

IN-SIK KANG

School of Earth and Environmental Sciences, Seoul National University, Seoul, South Korea

(Manuscript received 28 October 2010, in final form 27 February 2011)

ABSTRACT

Systematic relationships between aspects of intraseasonal variability (ISV) and mean state bias are shown in a number of atmospheric general circulation model (AGCM) simulations. When AGCMs are categorized as either strong ISV or weak ISV models, it is shown that seasonal mean precipitation patterns are similar among models in the same group but are significantly different from those of the other group. Strong ISV models simulate excessive rainfall over the South Asian summer monsoon and the northwestern Pacific monsoon regions during boreal summer. Larger ISV amplitude also corresponds closely to a larger ratio of eastward-to-westward-propagating variance, but no model matches the observations in both quantities simultaneously; a realistic eastward-to-westward ratio is simulated only when variance exceeds that observed. Three sets of paired simulations, in which only one parameter in the convection scheme is changed to enhance the moisture sensitivity of convection, are used to explore the common differences between the two groups in greater detail. In strong ISV models, the mean and the standard deviation of surface latent heat flux is greater, convective rain fraction is smaller, and tropical tropospheric temperatures are lower compared to weak ISV models. The instantaneous joint relationships between daily gridpoint relative humidity and precipitation differ in some respects when strong and weak ISV models are compared, but these differences are not systematic enough to explain the differences in ISV amplitude. Conversely, there are systematic differences in the frequency with which specific values of humidity and precipitation occur. In strong ISV models, columns with a higher saturation fraction and rain rate occur more frequently and make a greater contribution to total precipitation.

Corresponding author address: Daehyun Kim, Lamont-Doherty Earth Observatory, Columbia University, 61 Route 9W, Palisades, NY 10964.
E-mail: dkim@ldeo.columbia.edu

1. Introduction

It is well known that over the tropics, there is significant variability of rainfall fluctuating with time scales shorter than a season, known as intraseasonal variability

(ISV). The dominant mode of tropical ISV is the Madden–Julian oscillation (MJO; Madden and Julian 1971, 1972), characterized by its planetary spatial scale of wavenumbers 1–3, low-frequency period of 30–60 days, and its prominent eastward propagation over the entire globe. As it modulates deep convection over the tropics, the MJO has large impacts on a wide variety of climate phenomena across different spatial and temporal scales. Some examples include the onsets and breaks of the Indian and Australian summer monsoons (e.g., Yasunari 1979; Wheeler and McBride 2005), the formation of tropical cyclones (e.g., Liebmann et al. 1994; Maloney and Hartmann 2000b,a; Bessafi and Wheeler 2006), and the onset of some El Niño events (e.g., Takayabu et al. 1999; Bergman et al. 2001; Kessler 2001).

Simulation of the MJO, however, has been a difficult test for most climate models, from the Atmospheric Model Intercomparison Project (AMIP; Slingo et al. 1996) to the recent Coupled Model Intercomparison Project phase 3 (CMIP3; Lin et al. 2006). Lin et al. (2006) showed that only two models in CMIP3 had MJO variance comparable to observations, with even those lacking realism in many other MJO features.

At the same time, many previous studies have shown that simulation of the MJO can be improved by changing aspects of the cumulus parameterization of the GCM. The changes that have been made to this end differ in detail but have in common inhibited cumulus convection (Tokioaka et al. 1988; Wang and Schlesinger 1999; Maloney and Hartmann 2001; Lee et al. 2003; Zhang and Mu 2005 (ZM05); Lin et al. 2008), an improved representation of downdrafts and rain reevaporation (Maloney and Hartmann 2001), and modified convective closures (Zhang and Mu 2005).

When we change a given model to improve one aspect of the climate simulation, it usually produces changes in other aspects also because of complex interactions among model components. Wang and Schlesinger (1999) and Slingo et al. (1996) documented the relationships between the strength of ISV and the mean state in uncoupled atmospheric general circulation models (AGCMs). Slingo et al. (1996) showed that mean precipitation tends to be more confined to high sea surface temperature (SST) regions in models that simulate stronger ISV. Similarly, Wang and Schlesinger (1999) suggested, using various versions of one AGCM, that a strong relationship between precipitation and SST is necessary to properly simulate ISV. Because the above studies focused on the boreal winter season, they found that mean precipitation is more confined to the South Pacific convergence zone (SPCZ) region when a model simulates strong ISV.

In general, climate models are developed for the primary purpose of simulating climate variability and change

on time scales from interannual to decadal and longer, including projections of long-term change due to greenhouse gas forcing. Accordingly, features of the climate that are manifest in long-term averages are often perceived as more important than intraseasonal variability. We document here something that we suspect is known to many modeling groups and that may be the reason for poor MJO simulation in many models: it is difficult to improve a model's MJO simulation without degrading its mean state simulation, because of a systematic relationship between them.

In this study, we show that there is a systematic relationship between the strength of boreal winter ISV and both boreal summer and winter mean state biases in 10 AGCM simulations. Our focus is on boreal winter ISV—dominated by the MJO—rather than on boreal summer ISV. Nonetheless, our analysis of mean state biases focuses on boreal summer as well as winter. Models with strong boreal winter ISV have mean biases that are even larger during boreal summer than during winter. We view these as interesting, not because there is any direct relationship between the boreal summer mean state and boreal winter ISV, but simply because we are interested in the broader question of how changes in different aspects of climate simulations covary with changes in model physics.

Section 2 describes the participating models and the data used for validation. The relationship between simulations of the ISV and the mean state from 10 different AGCM simulations is shown in section 3. A diagnostic analysis is used to find common differences between strong ISV and weak ISV models in the latter part of section 3. A summary and conclusions are given in section 4.

2. Participating models and data

a. Participating models

Ten different climate simulations from five different AGCMs are used in this study. Table 1 summarizes the model configurations and simulation details, including the convection scheme used in each model, the horizontal and vertical resolutions, and the simulation period. All simulations are integrated for at least 10 yr. All 10 simulations are used in the first part of the next section, to show the general relationship between ISV and the mean state. Then we concentrate on three pairs of simulations with Atmospheric Model, version 2 (AM2; Geophysical Fluid Dynamics Laboratory), SNU (Seoul National University GCM; Seoul National University), and CAM3.1R [Community Atmosphere Model, version 3.1R; National Center for Atmospheric Research (NCAR)], in which the same configurations are used

TABLE 1. Description of participating models. Model expansions and parent organizations are supplied in the text.

Model	Convection scheme	Version	Resolution	Period
AM2	RAS ^a	tok = 0.025 or 0.1	2.0° lat × 2.0° lon/L24	10 yr, with climatological SST
SNU	sRAS ^b	tok = 0.0 or 0.1	T42/L20	20 yr, 1 Jan 1986–31 Dec 2005
CAM3.1R	RAS ^a	evap = 0.05 or 0.6	T42/L26	10 yr, with climatological SST
CAM3 (NCAR)	ZM ^c	Neale et al. (2008; NRJ08)	1.9° lat × 2.5° lon/L26	20 yr, 1 Jan 1986–31 Dec 2005
		ZM05, as this was abbreviated above.	T42/L26	15 yr, 29 Jan 1980–23 Jul 1995
	SP ^d	Khairoutdinov et al. (2005)	T42/L26	19 yr, 1 Oct 1985–25 Dec 2005
GEOS5	RAS ^a	Rienecker et al. (2008) tok = 0.05	1° lat × 1.25° lon/L72	12 yr, 1 Dec 1993–30 Nov 2005

^a RAS: Relaxed Arakawa–Schubert (Moorthi and Suarez 1992).

^b sRAS: Simplified RAS (Numaguti et al. 1995).

^c ZM: Zhang and McFarlane (1995).

^d SP: Superparameterization (Khairoutdinov and Randall 2001).

except for one parameter in the cumulus parameterization. The Tokioka modification (Tokioka et al. 1988), which suppresses convective plumes with entrainment rates less than a threshold that varies inversely with planetary boundary layer (PBL) depth, is implemented in AM2 and SNU with different threshold values. In that modification, the threshold value is defined as $\mu_{\min} = \alpha/D$, where D is the depth of the PBL and α (tok in Table 1 and figures) is a nonnegative constant. The constant α , which determines the strength of triggering, is set to 0.025 and 0.1 in two different versions of AM2, while 0 and 0.1 are used in the SNU models. Rain reevaporation efficiency (evap) is modified in CAM3.1R from 0.05 to 0.6 in a model that also has a Tokioka-like minimum entrainment threshold of 0.0001 m^{-1} (which would correspond to $\alpha = 0.1$ for a PBL depth of 1 km) employed. Hannah and Maloney (2011) demonstrated the sensitivity of ISV in this model to the minimum entrainment threshold. The modifications have been shown to improve the ISV simulation in each model (Lin et al. 2008; Sobel et al. 2010). Considerable analysis of the simulated MJO dynamics has been performed for each of these three models, including sensitivity to the convective parameters described above (e.g., Maloney and Sobel 2004, Maloney et al. 2010 for CAM3.1R; Sobel et al. 2010 for AM2; Lee et al. 2003, Lin et al. 2008 for SNU).

b. Observational data

We validate the simulations of rainfall against the Global Precipitation Climatology Project (GPCP; Huffman et al. 2001) product version 1.1. The tropospheric zonal winds and temperature are from the National Centers for

Environmental Prediction (NCEP)–NCAR reanalysis data (Kalnay et al. 1996) and the reanalysis from the European Centre for Medium-Range Weather Forecasts (ECMWF) Re-Analysis-Interim (ERA-Interim) (Simmons et al. 2007). The Special Sensor Microwave Imager (SSM/I)–Tropical Rainfall Measuring Mission (TRMM) Microwave Imager (TMI) combined precipitable water data are also used.

3. Results

a. Results from 10 simulations with six models

Figure 1 shows the November–April standard deviation of 20–100-day bandpass-filtered precipitation. It is clear from this figure that stronger ISV of precipitation is observed in simulations in the right column than those in the left column. Based on Fig. 1, we cluster the simulations into two groups: strong ISV (right column) and weak ISV (left column) models (the separation is clear in terms of area-averaged standard deviation over the tropics in Fig. 3). The increased variance does not necessarily translate into more realism, however. All simulations in the right column overestimate the amplitude of ISV, as measured by the variance, to varying extents (we can make the same separation based on boreal summer data; the resulting pattern is not shown, but area-averaged values are shown in Fig. 6a).

A significant difference between the two groups is also found in the propagation direction of ISV. Figure 2 shows the lag correlation of 10°S – 10°N -averaged 20–100-day bandpass-filtered 850-hPa zonal wind against a reference point in the equatorial Indian Ocean (IO; 5°S – 5°N , 75° – 90°E). The intraseasonal anomalies of

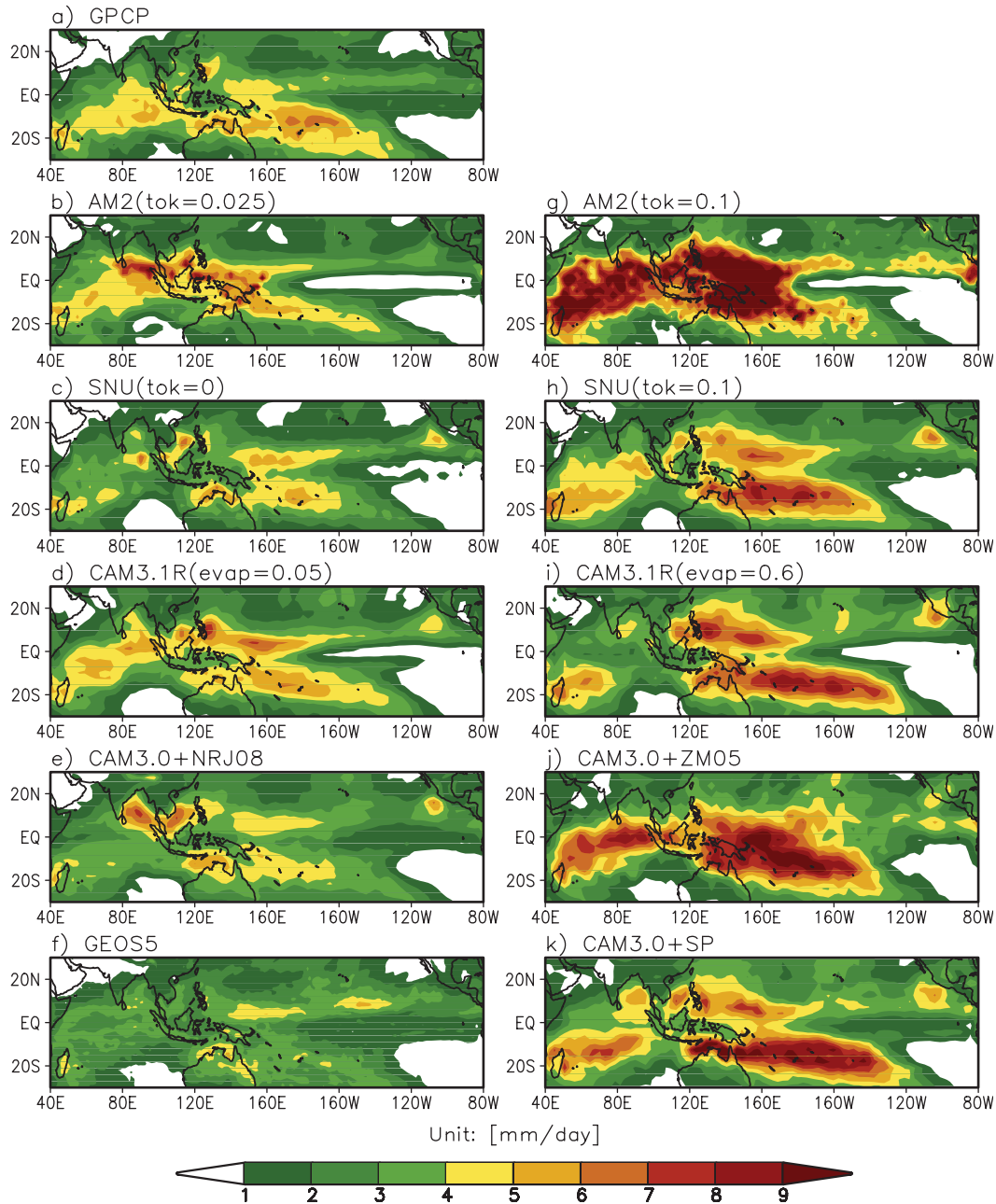


FIG. 1. November–April standard deviation of 20–100-day bandpass-filtered precipitation (mm day^{-1}) for (a) GPCP, (b) AM2 (tok = 0.025), (c) SNU (tok = 0.0), (d) CAM3.1R (evap = 0.05), (e) CAM3 + NRJ08, (f) GEOS5, (g) AM2 (tok = 0.1), (h) SNU (tok = 0.1), (i) CAM3.1R (evap = 0.6), (j) CAM3.0 + ZM05, and (k) CAM3 + SP.

zonal wind propagate from west to east through the Indian Ocean in the two different reanalysis products (Figs. 2a and 2g). The eastward-propagating feature is well known as one of the basic characteristics of the MJO. The weak ISV models exhibit near-standing or westward propagation—opposite to what is observed. The strong ISV models simulate eastward propagation better than the weak ISV models. In AM2, SNU, and

CAM3.1R, modifications to the convection scheme to enhance the moisture sensitivity of convection result in an improvement of the eastward propagation, as reported in previous studies (Tokioka et al. 1988; Wang and Schlesinger 1999; Lin et al. 2008; Sobel et al. 2010).

In Fig. 3, the relationship between the strength of ISV and the dominant propagation direction of ISV is summarized in a scatter diagram. The strength metric

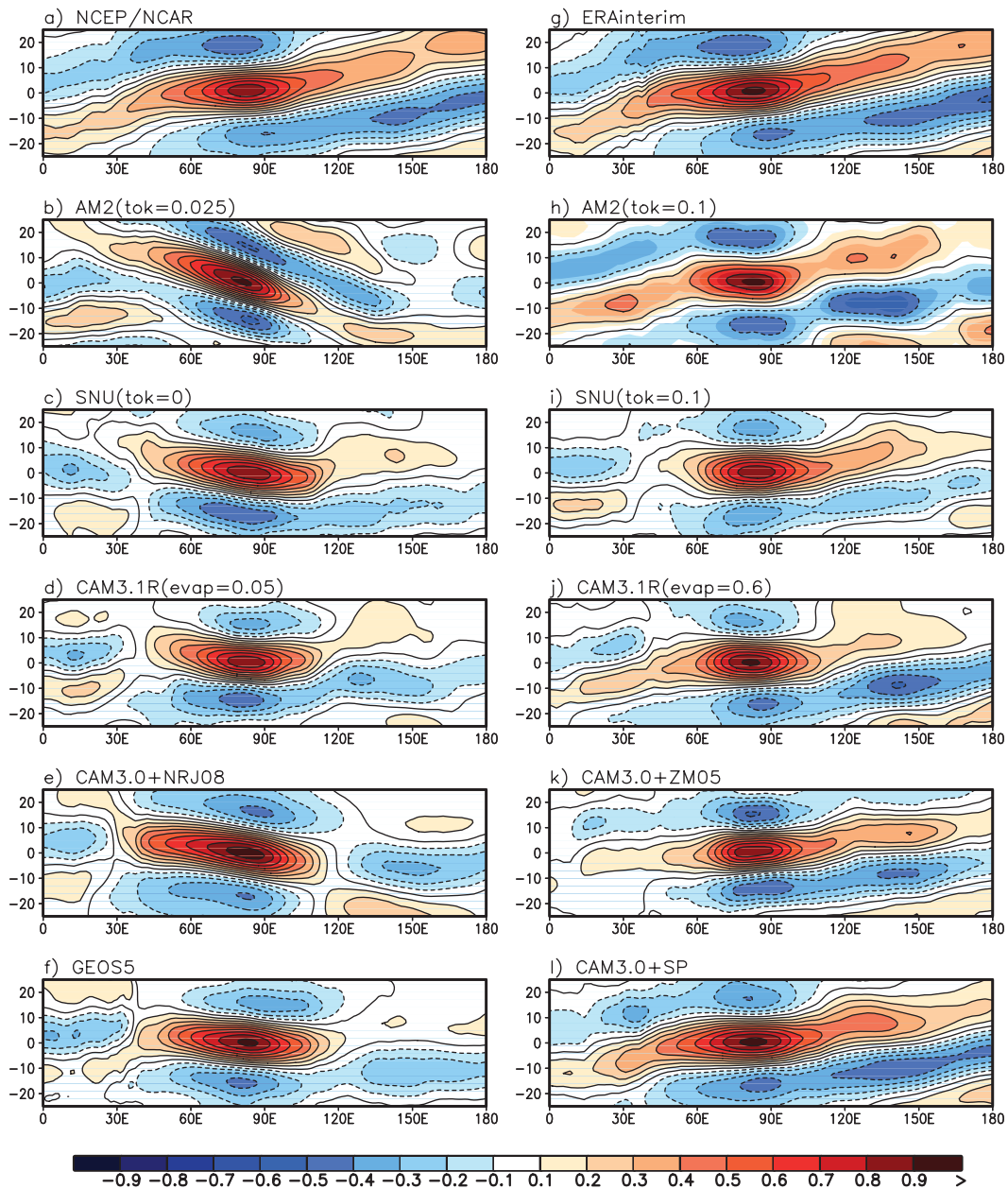


FIG. 2. November–April lag–longitude diagram of 10°N – 10°S -averaged intraseasonal 850-hPa zonal wind anomalies correlated against intraseasonal zonal wind anomalies at the IO (5°S – 5°N , 70° – 95°E averaged) reference point. (a) NCEP–NCAR, (b) AM2 (tok = 0.025), (c) SNU (tok = 0.0), (d) CAM3.1R (evap = 0.05), (e) CAM3 + NRJ08, (f) GEOS5, (g) ERA-Interim, (h) AM2 (tok = 0.1), (i) SNU (tok = 0.1), (j) CAM3.1R (evap = 0.6), (k) CAM3 + ZM05, and (l) CAM3 + SP.

is obtained by averaging the standard deviation of 20–100-day filtered precipitation over the tropics (30°S – 30°N , 0° – 360°E). For the propagation direction metric, the eastward-to-westward ratio of ISV is calculated from space–time power spectra, by dividing the sum of the spectral power over eastward-propagating zonal wavenumbers 1–3 and a frequency range of 30–70 days by its westward-propagating counterpart. Figure 3 shows that

there is an approximate linear relationship between the two metrics. Overall, weak ISV models (open circles) underestimate the eastward-to-westward ratio metric compared to observations, although they reasonably simulate the magnitude of ISV. Note that all weak ISV models have smaller ISV magnitude than strong ISV models. Strong ISV models generally show eastward-to-westward ratios comparable to that of observations and larger than those

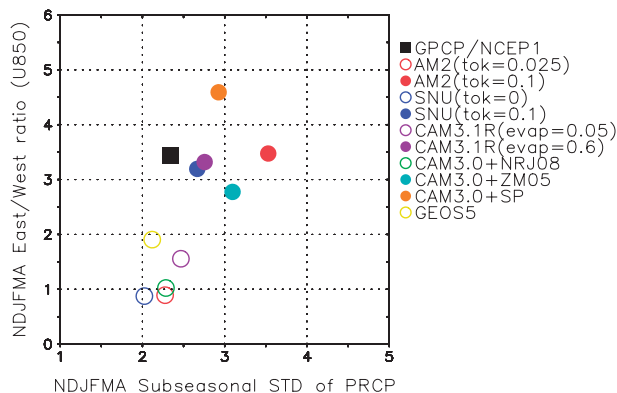


FIG. 3. Scatterplot of November–April standard deviation 20–100-day bandpass-filtered precipitation averaged over 30°S–30°N, 0°–360°E and the eastward-to-westward ratio, defined as the ratio of eastward-propagating spectral power (summation over wavenumbers 1–3, period 30–70 days) to that of its westward-propagating counterpart. Open (closed) circle represents the weak (strong) ISV model.

of the weak ISV models. We find striking the extent to which the relationship plotted for the models is compact and linear although simultaneously the observations deviate from it. When we construct a linear regression equation using model data ($y = 2.0023x - 2.8559$, where x is the tropics-averaged standard deviation and y is the eastward-to-westward ratio), the error of the regression equation to predict the observed eastward-to-westward ratio (~ 1.5) is about twice that of the averaged error against model data (~ 0.8), indicating that the observation point can be regarded as an outlier. Only one model [the superparameterized Community Atmosphere Model (SPCAM)] has a larger error (~ 1.7) than the observations. There is no model that simultaneously simulates the observed variance and eastward-to-westward ratio. Models with an eastward-to-westward ratio comparable to that observed tend to overestimate the variance. It seems that even if we are willing to accept significant degradation in the simulation of the mean state (as is shown below to occur in the strong ISV model), we are not yet able to produce a fully realistic MJO simulation.

To investigate the relationship between ISV characteristics and the mean state, May–October-averaged precipitation is shown in Fig. 4. As discussed in the introduction, we present mean state fields for this season—despite our focus on boreal winter ISV—because the boreal summer mean state biases are related to simulated boreal winter ISV amplitude across our multimodel ensemble in a particularly systematic way. In the Western Hemisphere, observed boreal summer mean precipitation is characterized by maxima in several locations, including the equatorial Indian Ocean, the northwestern

Pacific, west of the India and Indochina Peninsulas, west of the Philippines, and east of Papua New Guinea (Fig. 4). While most of these observed maxima are captured in most simulations—with different fidelities—there are similarities in the precipitation patterns within the strong and weak ISV model groups. For example, in weak ISV models, precipitation maxima over the central Pacific are prominent with a compensating dry bias over the western Pacific (WP). In 4 out of 5 strong ISV models, a zonally elongated precipitation pattern is simulated from 60° to 160°E and from 10° to 20°N (except AM2). This is clearly distinguishable from the intertropical convergence zone (ITCZ), which extends from 160°E to the western boundary of the American continent at about 5°N.

When we focus on the WP (5°S–15°N, 120°–160°E) and equatorial IO (15°S–5°N, 60°–95°E) regions, we find a clear difference between the strong and weak ISV groups. Weak ISV models simulate stronger (weaker) precipitation in the IO (WP) than the strong ISV models in the right column (Fig. 4). Compared to observations, the weak ISV models generally have a wet (dry) bias over the IO (WP) region, while the signs of the biases are reversed in the right column. Although mean precipitation is generally higher over the IO region for the weak ISV models, the subseasonal variability of precipitation is stronger there in the strong ISV models. This implies that the increase of subseasonal variability is not a result of higher mean rainfall in this region. A systematic difference between strong and weak ISV models groups is also observed during boreal winter. There is a tendency in strong ISV models for precipitation in the SPCZ to be stronger, while rainfall in the eastern Pacific (EP) ITCZ is weaker than in weak ISV models (Fig. 5).

Figure 6 summarizes the relationship between ISV and mean state simulation in a scatter diagram, with boreal summer on the left and boreal winter on the right. The transverse axes in Fig. 6 show the seasonally stratified ISV strength metric, while the ordinate axes show a May–October (Fig. 6a) and November–April (Fig. 6b) mean precipitation index, defined as the mean precipitation difference between two selected regions (see caption). It is shown in Fig. 6 that a model with stronger ISV tends to simulate a larger difference of mean precipitation between the selected regions in both seasons, with even more precipitation occurring over the wetter WP warm pool. A linear relationship between ISV strength and mean precipitation index in Fig. 6 demonstrates that there is a systematic relationship between ISV characteristics and mean state bias simulated in 10 different AGCM simulations. Strengthening the magnitude of ISV and improving the propagation direction of ISV results in a degradation of the mean state at least by this metric (an increase of

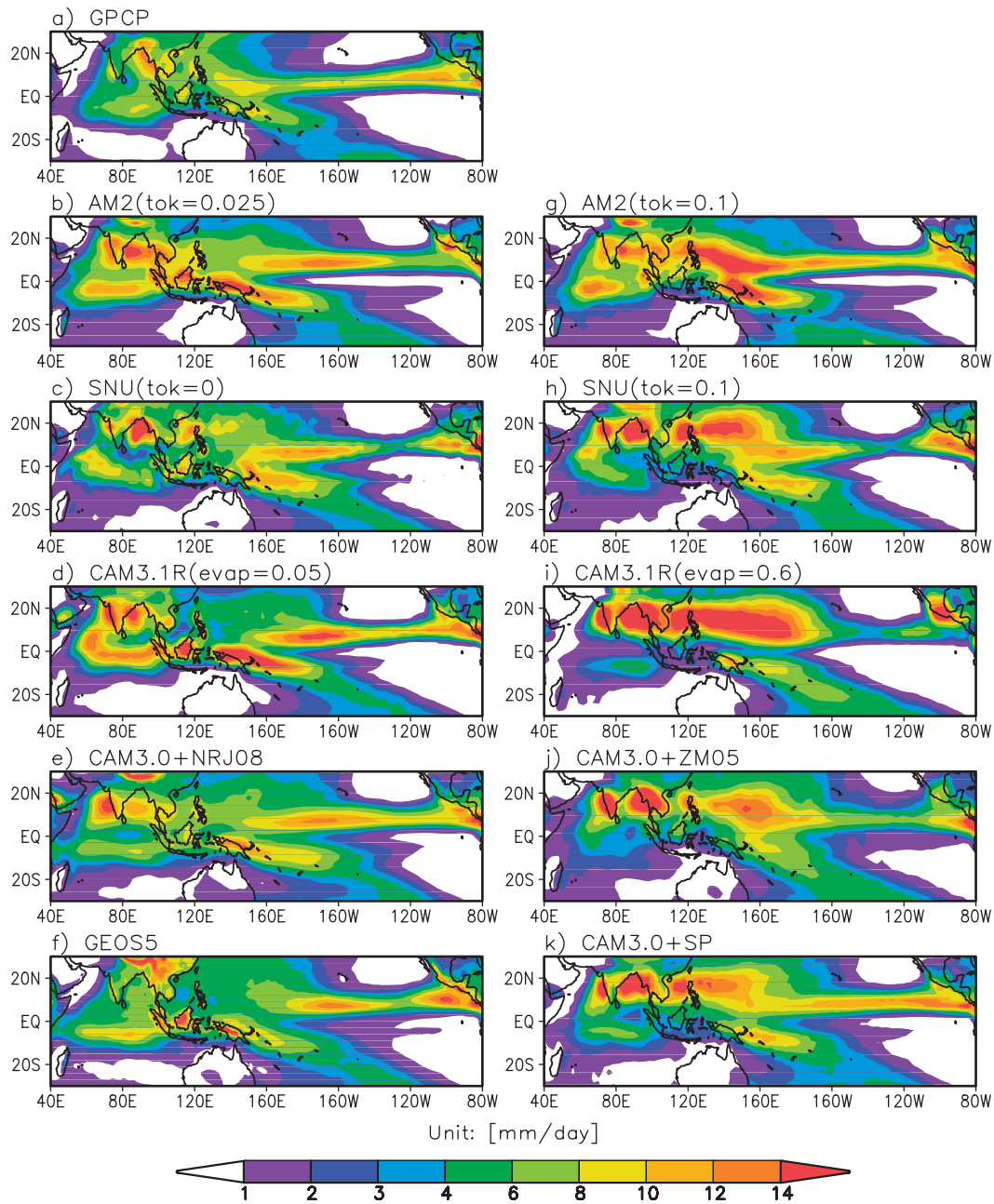


FIG. 4. As in Fig. 1, but for May–October mean precipitation (mm day^{-1}).

the difference of the mean precipitation index from its observed value).

b. Detailed analysis of three model pairs

Next, we conduct a more detailed search for common features that distinguish strong ISV models from weak ISV models using three sets of paired simulations with AM2, SNU, and CAM3.1R.

Luo and Stephens (2006) examined the excessive boreal summer mean precipitation over the western

Pacific in SPCAM. They suggested an anomalously strong convection–wind–evaporation feedback, partly caused by the two-dimensional geometry of the cloud-resolving model implemented in SPCAM, was the cause of the precipitation bias. We also find that evaporation is larger in the strong ISV models than in the weak ISV models. Figure 7 shows a difference map (strong ISV version minus weak ISV version) of May–October precipitation and evaporation in each pair of simulations. There is an enhancement of surface latent heat flux in

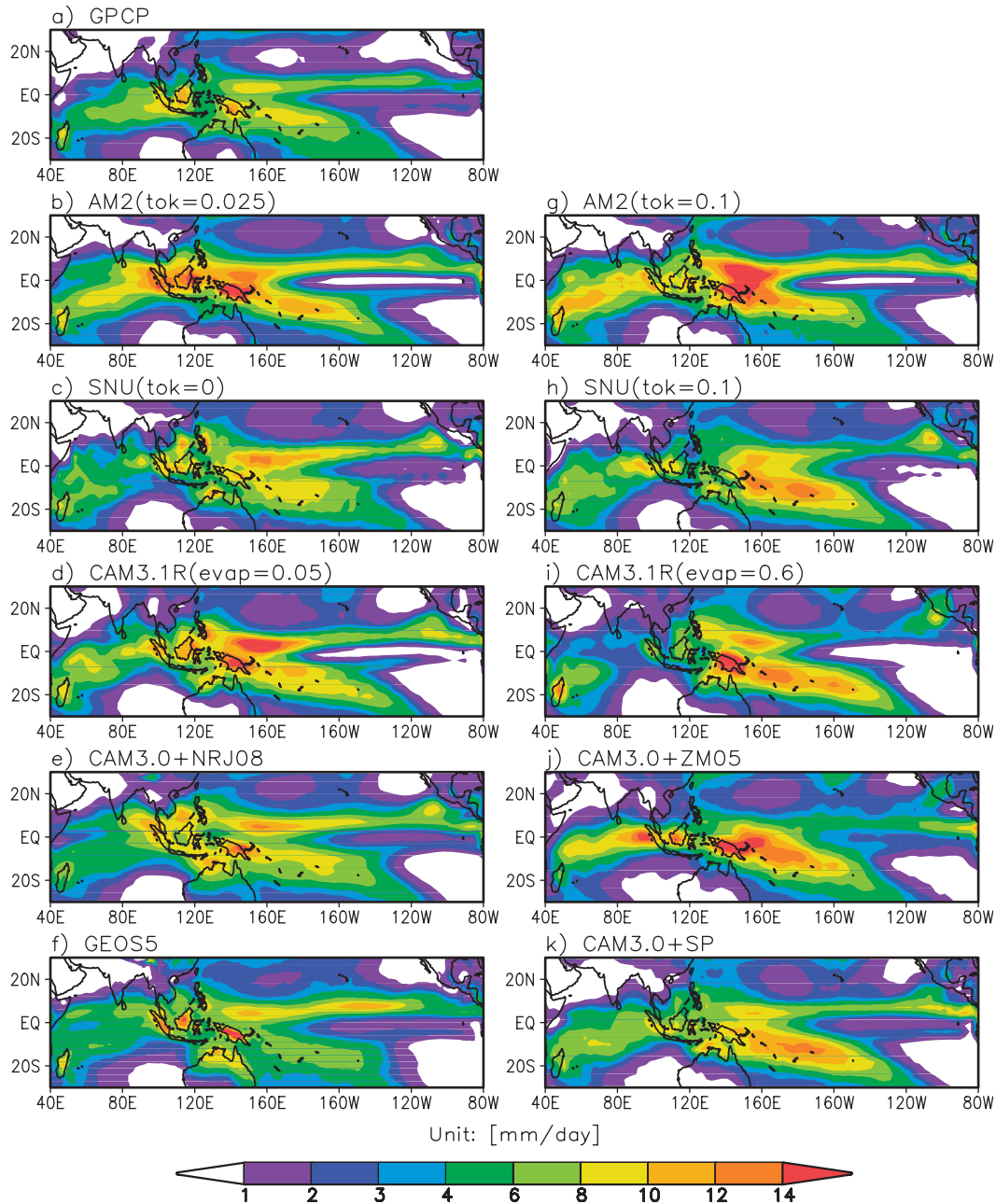


FIG. 5. As in Fig. 4, but for November–April mean precipitation (mm day^{-1}).

the regions where precipitation is increased (Fig. 7). Furthermore, the increase of mean latent heat flux is accompanied by an increase in variance at subseasonal time scales (Fig. 8). The argument about a too-strong convection–wind–evaporation feedback by Luo and Stephens (2006) is consistent with our results. However, the additional reasoning that the cloud-resolving model geometry causes the excessive feedback is not supported by the results here, because a similar bias appears in models with conventional parameterizations. Our

results demonstrate that the problem is not a specific one for models with cloud-resolving models embedded in each large-scale grid box, but rather is a common symptom of models that overestimate the strength of ISV. Some of the excessive strength of this feedback is likely due to the fixed SST lower boundary. We expect this feedback to be weaker in models run over a dynamic ocean or a slab ocean, since in such models the increased latent heat flux would result in a cooling of the ocean surface and consequent suppression of convection.

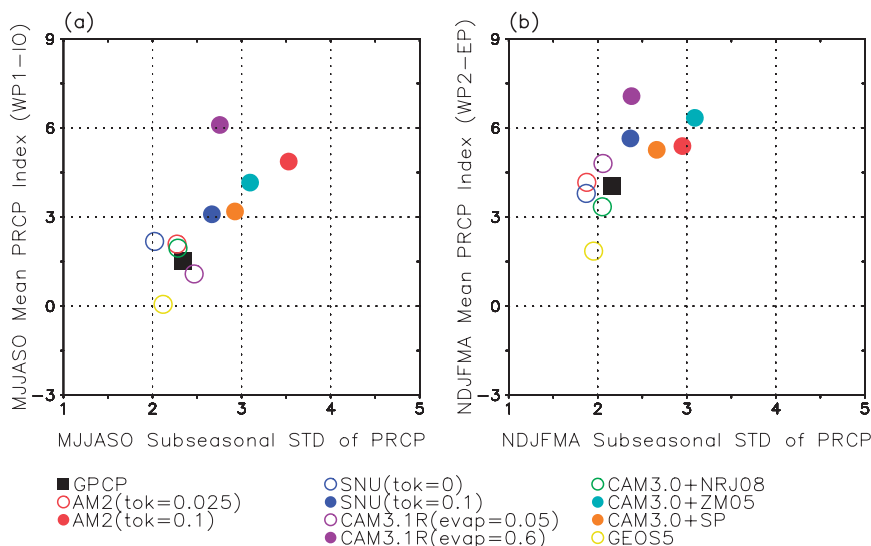


FIG. 6. Scatterplots of (a) May–October standard deviation of 20–100-day filtered precipitation averaged over 30°S – 30°N , 0° – 360°E and the May–October mean precipitation index, which is defined as averaged precipitation over WP1 (5°S – 20°N , 120° – 160°E) minus IO (15°S – 5°N , 60° – 95°E), and (b) November–April standard deviation of 20–100-day filtered precipitation averaged over 30°S – 30°N , 0° – 360°E and November–April mean precipitation index defined as averaged precipitation over WP2 (20°S – 0° , 140°E – 180°) minus EP (0° – 10°N , 20° – 80°W). Open (closed) circle represents weak (strong) ISV model.

The fraction of rainfall produced by the convection scheme (as opposed to grid-scale saturation) is expected to be smaller in a strong ISV model compared to a weak ISV one if the minimum entrainment rate threshold or the rain reevaporation efficiency has been increased in

the former relative to the latter. This expectation is borne out by Fig. 9, which shows difference maps (strong ISV minus weak ISV) of the annual mean convective rain fraction for the three model pairs. In Fig. 9, AM2 shows the convective rain fraction reduced by more than 50%

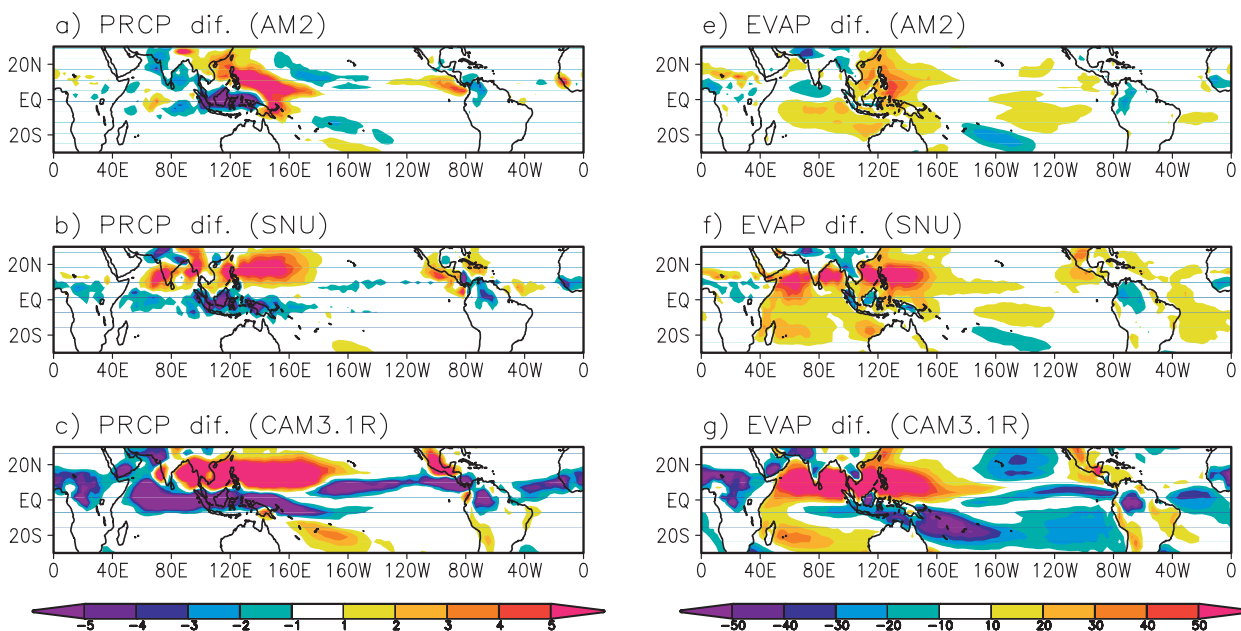


FIG. 7. (a)–(c) Difference map of May–October precipitation (mm day^{-1}) for (a) AM2, (b) SNU, and (c) CAM3.1R. (d)–(f) Difference map of May–October evaporation (W m^{-2}) for (e) AM2, (f) SNU, and (g) CAM3.1R.

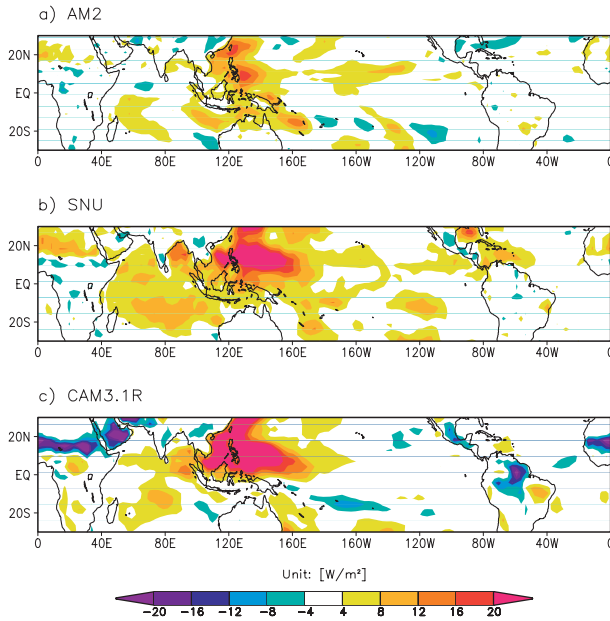


FIG. 8. Difference map of May–October standard deviation of 20–100-day filtered evaporation for (a) AM2, (b) SNU, and (c) CAM3.1R.

over the western Pacific region, where mean precipitation increases significantly. SNU and CAM3.1R also show an overall reduction of convective rainfall fraction over the tropics.

Figure 10 shows a scatterplot of the standard deviation of intraseasonal precipitation anomalies versus tropical mean tropospheric temperature, defined as the average in pressure coordinates from the surface to 100 hPa. Since all models are run over nearly identical fixed SSTs, the differences in the tropospheric temperatures in this figure come primarily from the upper troposphere. Figure 10 shows that the strength of ISV is linearly related to the tropical mean tropospheric temperature with a negative slope. Observations lie in the middle of the spread of the simulations. The CAM3.1R models have similar tropospheric temperature, as well as similar strength of ISV to each other. With a smaller convective rainfall fraction, we may expect that the convective heating in the upper troposphere will be reduced, as greater entrainment forces convection to be shallower. Reduced diabatic heating by convection results in a reduced temperature of the upper troposphere. This destabilizes the atmospheric column, but this is counteracted by the increased inhibitive effect of subsaturation in the free troposphere. Reduced cloud height with reduced fraction of convective rainfall also enhances radiative cooling by decreasing the greenhouse effect of high clouds. A full analysis of the tropical static stability in the strong ISV and weak ISV versions of the SNU model and its effect

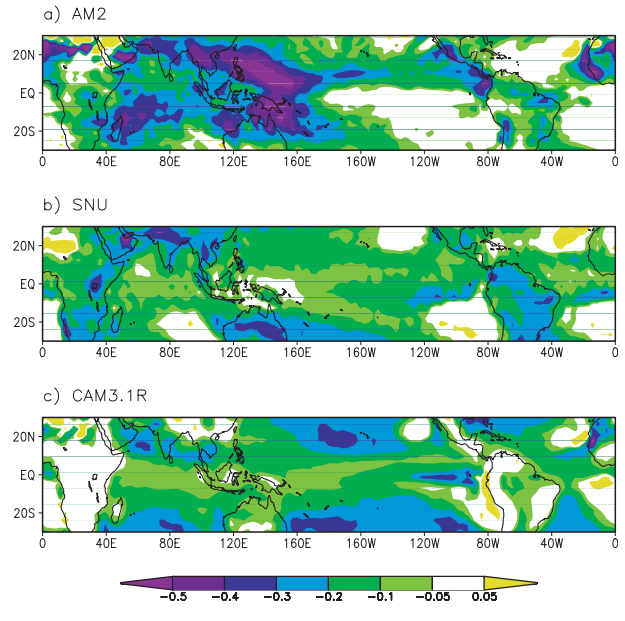


FIG. 9. Difference map of annual mean convective rain fraction for (a) AM2, (b) SNU, and (c) CAM3.1R.

on the speed of convectively coupled Kelvin waves was performed in Frierson et al. (2010).

Using a reduced-complexity model of the tropical atmosphere, Raymond (2001) suggested that the local relationship between moisture and precipitation is crucial for the MJO to be sustained. In his model, which simulates the MJO, precipitation is inversely proportional to saturation deficit, the difference between column moisture and its saturated value (the latter minus the former). The relationship between column moisture and precipitation in satellite observations was investigated by Bretherton et al. (2004), who showed that, on monthly and daily time scales, the mean value of precipitation

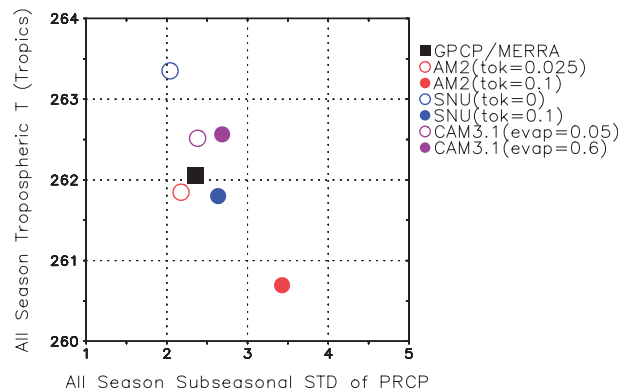


FIG. 10. Scatterplots of all-season standard deviation averaged over 30°S–30°N, 0°–360°E and all-season mean tropospheric temperature averaged over 30°S–30°N, 0°–360°E. Open (closed) circle represents the weak (strong) ISV model.

occurring at a given column relative humidity (the ratio of column moisture to its saturated value) increases exponentially when the latter is larger than some critical value. Peters and Neelin (2006) and Neelin et al. (2009) examined the relationship more thoroughly. They found that the relationship between precipitable water and precipitation could be generalized when precipitable water was rescaled by critical precipitable water, which was a function of tropospheric temperature (though one not, as one might have expected, identical to the saturation column water vapor). Based on the above modeling and observation studies, it is reasonable to think that the observed moisture–precipitation relationship is one of the characteristic features that should be simulated correctly to replicate the MJO accurately, though a comprehensive theory for such a linkage does not yet exist.

In recent studies, the local moisture–precipitation relationship has been suggested as a diagnostic tool to distinguish strong MJO models from weak MJO models. Precipitation composites based on saturation fraction from daily gridpoint data, used in Zhu et al. (2009), and composites of vertically resolved relative humidity against precipitation, used in Thayer-Calder and Randall (2009), were shown in those studies to be useful for this purpose. Comparing CAM3 and SPCAM, Zhu et al. (2009) and Thayer-Calder and Randall (2009) showed that more realistic local relationships between column moisture and precipitation are found in SPCAM, which also has a better simulation of the MJO than CAM3.

Figure 11 shows the observed and simulated daily gridpoint relative humidity composite based on precipitation for strong and weak ISV models. The x axis of the plot is \log_{10} of precipitation (mm day^{-1}). Thayer-Calder and Randall (2009) showed that in observations and in a model that simulates the MJO well (SPCAM), there is a gradual moistening of the troposphere accompanied by a deepening of the area of high relative humidity. In Fig. 11, SNU and CAM3.1R show an increase of relative humidity in the mid- and lower troposphere at high rain rates in the strong ISV version (Figs. 11g and 11j), consistent with the results of Thayer-Calder and Randall (2009). The increase of relative humidity in the strong ISV version is not clear in AM2 (Fig. 11d). Contours (dashed lines) of 75% are drawn to highlight the gradual deepening of the area of high relative humidity. Overall, the contours have slopes more similar to that observed in the strong ISV models than in the weak ISV models. However, this diagnostic does not explain all the differences because, for example, the SNU model with a minimum entrainment rate threshold of 0.1 has stronger ISV and a higher eastward-to-westward ratio than the AM2 model with a threshold of 0.025, although

the slope of the 75% contour seems to be more similar to that observed in the AM2 model.

Similar to Zhu et al. (2009), precipitation is composited based on the saturation fraction over the warm pool region in Fig. 12 (top panels). In this diagram, we used the ERA-Interim data for temperature and the SSM/I–TMI combined data for precipitable water to calculate the saturation fraction. For precipitation, the GPCP product version 1.1 is used. In general, composited precipitation is near zero until the saturation fraction reaches some critical value, after which precipitation increases rapidly. When we compare weak ISV models (dashed line) to strong ISV models (solid line), however, the three sets of models show three distinct types of behavior in terms of the critical value and the slope of the curve for a saturation fraction larger than that value. Here, the critical value is loosely defined as the point after which the slope of the curve increases significantly. In AM2, the slope from the strong ISV version is steeper than that of the weak ISV version, while both show similar critical values. The two versions of the SNU model have similar slopes and critical values. The critical value is significantly increased in CAM3.1R with larger convective rain reevaporation efficiency. The different behavior of the relationships between moisture and precipitation are interesting because the convection schemes used in these three models are similar (Table 1).

The probability density function (PDF) of the saturation fraction is also shown in Fig. 12 (middle panel). In observations (black line), the peak of the PDF is near 0.8, after which the PDF drops quickly. The peaks of the PDF in the AM2 models are similar to the observed value, while the SNU models have peaks near 0.6. The two different versions of CAM3.1R show quite different shapes of the PDF. The most frequent value of the saturation fraction moves from near 0.7 in the weak ISV version to about 0.9 in the strong ISV version. In all three models, the occurrence of high saturation fractions (right tail of the curve) increases in the strong ISV version compared to the weak ISV version. When the composited precipitation is weighted by the PDF of the saturation fraction (Fig. 8, bottom panel), the difference between the strong and weak ISV models becomes more similar among the three models. The PDF-weighted composited precipitation can be regarded as the total amount of precipitation from columns with a given saturation fraction value divided by the total number of samples used in the PDF calculation, the sum of which is the time- and domain-mean precipitation. It is clear in Fig. 12 that the amount of precipitation that occurs at high saturation fraction increases with stronger ISV in all three models, indicating a larger contribution from columns with high saturation fraction to the total amount of precipitation.

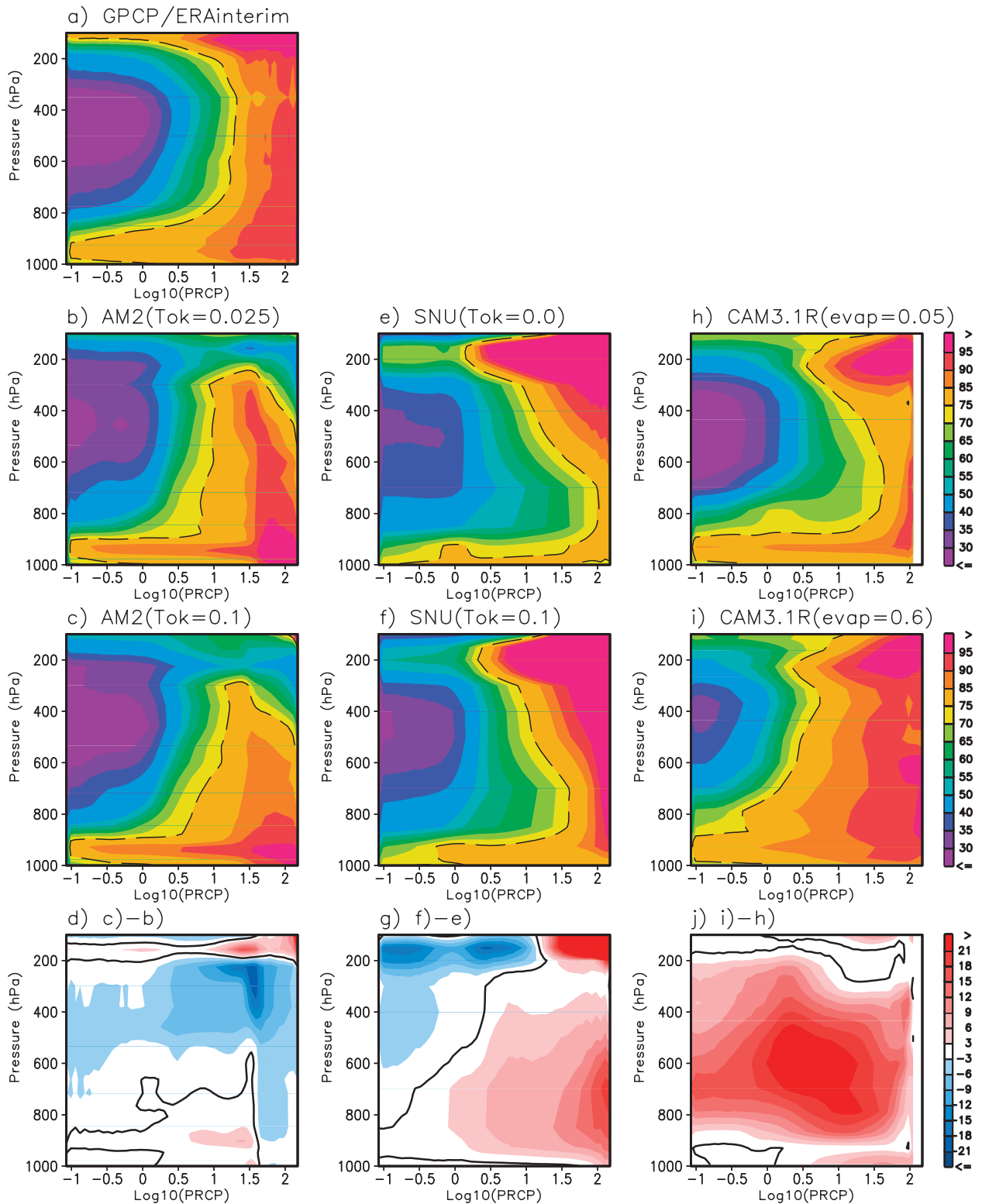


FIG. 11. Composite vertical profile of relative humidity based on precipitation rate for (a) GPCP/ERA-Interim, (b) AM2 (tok = 0.025), (c) AM2 (tok = 0.1), (e) SNU (tok = 0.0), (f) SNU (tok = 0.1), (h) CAM3.1R (evap = 0.05), and (i) CAM3.1R (evap = 0.6). Difference between strong and weak ISV models is shown in (d) AM2, (g) SNU, and (j) CAM3.1R. Precipitation rate is plotted on a log scale, with the relative humidity averaged for each bin shown on the x axis. All-season data are analyzed over 20°S–20°N, 40°E–180°.

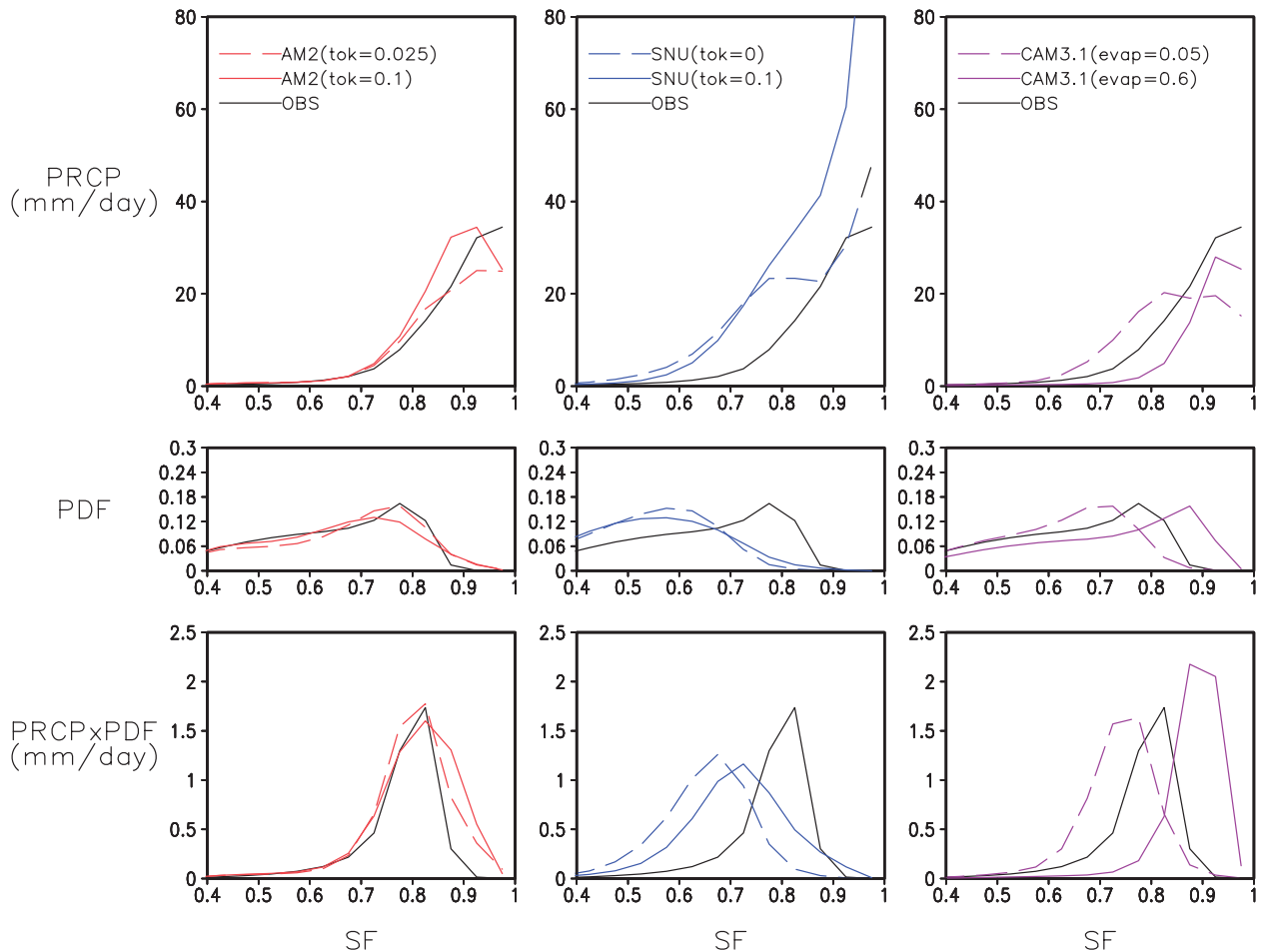


FIG. 12. (top) Precipitation composite based on saturation fraction. (middle) PDF of saturation fraction, (bottom) PDF-weighted precipitation. Points over the WP (0° – 20° N, 130° E– 180°) are used in calculations. All-season data are used.

Considered together, the plots shown in Figs. 11 and 12 suggest that the joint relationship between humidity and precipitation need not differ in a systematic way between strong and weak ISV models. This is somewhat contrary to expectations based on, for example, previous studies that have demonstrated some correspondence between the shape of the precipitation–saturation fraction curve and the simulation of ISV (e.g., Zhu et al. 2009).

4. Summary and conclusions

We used 10 different AGCM simulations to investigate the systematic relationships between ISV simulations and mean state bias. The 10 models are clustered into two groups in terms of the strength of their ISV, which is defined as the area-averaged standard deviation of ISV over the tropics.

The strong ISV models have magnitudes of ISV stronger than those of the weak ISV models and of observations (Fig. 3). The observed value is in between the

two model groups. The eastward-to-westward ratio and variance of ISV are closely related in these models; the eastward-to-westward ratios of the strong ISV models are larger than those of the weak ISV models and closer to the observed value. However, observations deviate from the simulated relationship between these two ISV properties, having larger eastward-to-westward ratio for the same variance as in the simulations.

It is shown that the pattern of boreal summer/winter mean precipitation is closely related to the strength of ISV (Fig. 6). The strong ISV models show a wet (dry) bias over the western Pacific (equatorial Indian Ocean) during boreal summer, while the signs of the biases are reversed in the weak ISV models. Similarly, during boreal winter, the amount of simulated precipitation in the SPCZ (ITCZ) region is larger (smaller) in the strong ISV models than in weak ISV models. Therefore, in strong ISV models, the strong precipitation is concentrated in the warmest ocean region (the western Pacific during boreal summer and the SPCZ region during

boreal winter), with compensating regions of decreasing precipitation (equatorial Indian Ocean during boreal summer and the ITCZ region during boreal winter). It is speculated here that the concentration of rainfall in the warmest ocean region is a consequence of enhancing the moisture–convection relationship (e.g., Figure 11). How the compensating region is determined, however, is not clear at this stage and needs further investigation.

Three sets of paired simulations (AM2, SNU, CAM3.1R), in which only one parameter in the convection scheme is changed to enhance the moisture sensitivity of convection, are used to find the common differences between the two groups. The mean and variance of the surface latent heat flux is increased in the strong ISV versions, consistent with the hypothesis that the wind–evaporation feedback is too strong in these models. The annual mean convective rain fraction is reduced in the strong ISV versions in all models, presumably as a direct result of the modifications implemented in the convective schemes to increase their sensitivity to environmental moisture. Relative humidity composites based on precipitation are also examined. Although strong ISV versions tend to represent the gradual deepening of the high relative humidity layer as a function of precipitation better compared to weak ISV versions, it is hard to explain the intermodel differences using this diagnostic. Differences between weak and strong ISV versions in the composited relationship between precipitation and the saturation fraction are not consistent across the three model pairs. Conversely, there is a consistent difference in the frequency distributions of the saturation fraction and precipitation. In strong ISV models, high values of saturation fraction and precipitation occur more frequently and make a greater contribution to the total precipitation.

Previous studies have shown that the strength of ISV simulated by GCMs can be controlled through modifications to the convection scheme. When convection is made more sensitive to environmental moisture, ISV becomes stronger. This method is often used to improve a model's ability to represent the MJO, the dominant mode of ISV in the tropics. Recent intercomparison studies, however, have demonstrated that most GCMs involved in the Fourth Assessment Report (AR4) of the Intergovernmental Panel on Climate Change (IPCC) have poor MJOs (Lin et al. 2006). The systematic relationships shown here between ISV characteristics and mean state bias may partly explain the current situation in which poor ISV models are used operationally, even though modelers know how to improve ISV. Presumably, the most important purpose of most operational climate models is long-term climate projection, for which a realistic mean climate is a higher priority than intraseasonal variability.

The models used in this study are atmosphere-only models, in which sea surface temperature is prescribed as a boundary condition. When sea surface temperature is prescribed, positive moisture–convection feedbacks over the warm pool produce excessive rainfall there. This is in part because of the lack of negative feedback mechanisms (e.g., reduced shortwave radiation and enhanced latent heat flux leading to reduced surface temperature) in the AGCMs. Stan et al. (2010) showed that excessive mean precipitation over the western Pacific during boreal summer disappears when the SPCAM is coupled to an ocean model. Sperber and Annamalai (2008) showed in a set of coupled GCMs that there was not a systematic relationship between the amplitude of boreal summer ISV and mean state biases. These results as well as ours suggest that air–sea coupling may change the relationship between ISV strength and mean state bias.

Acknowledgments. Components of this work were developed and discussed as part of the activities of the YOTC MJO Task Force. We thank Dr. Suzana Camargo for kindly providing scripts to generate the SSM/I–TMI combined precipitable water data. The ERA-Interim data used in this study have been provided by the ECMWF data server. This work was supported by NASA Grant NNX09AK34G (DK, AHS) and NOAA Grant NA08OAR4320912 (AHS, EDM, DMWF). This work was also supported by the Climate and Large-Scale Dynamics Program of the National Science Foundation under Grants ATM-0832868 and ATM-1025584 (EDM). ISK was supported by the Korea Meteorological Administration Research and Development Program under Grant CATER_2006-4206 and the second stage of the Brain Korea 21. DMWF was supported by NSF Grants ATM-0846641 and ATM-0936059.

REFERENCES

- Bergman, J. W., H. H. Hendon, and K. M. Weickmann, 2001: Intraseasonal air–sea interactions at the onset of El Niño. *J. Climate*, **14**, 1702–1719.
- Bessafi, M., and M. C. Wheeler, 2006: Modulation of south Indian Ocean tropical cyclones by the Madden–Julian oscillation and convectively coupled equatorial waves. *Mon. Wea. Rev.*, **134**, 638–656.
- Bretherton, C. S., M. E. Peters, and L. E. Back, 2004: Relationships between water vapor path and precipitation over the tropical oceans. *J. Climate*, **17**, 1517–1528.
- Frierson, D. M. W., D. Kim, I.-S. Kang, M.-I. Lee, and J.-L. Lin, 2010: Structure of AGCM-simulated convectively coupled Kelvin waves and sensitivity to convective parameterization. *J. Atmos. Sci.*, **68**, 26–45.
- Hannah, W. M., and E. D. Maloney, 2011: The role of moisture–convection feedbacks in simulating the Madden–Julian oscillation. *J. Climate*, **24**, 2754–2770.

- Huffman, G. J., R. F. Adler, M. M. Morrissey, D. T. Bolvin, S. Curtis, R. Joyce, B. McGavock, and J. Susskind, 2001: Global precipitation at one-degree daily resolution from multisatellite observations. *J. Hydrometeorol.*, **2**, 36–50.
- Kalnay, E., and Coauthors, 1996: The NCEP/NCAR 40-Year Reanalysis Project. *Bull. Amer. Meteor. Soc.*, **77**, 437–471.
- Kessler, W. S., 2001: EOF representations of the Madden–Julian oscillation and its connection with ENSO. *J. Climate*, **14**, 3055–3061.
- Khairoutdinov, M. F., and D. A. Randall, 2001: A cloud resolving model as a cloud parameterization in the NCAR Community Climate System Model: Preliminary results. *Geophys. Res. Lett.*, **28**, 3617–3620.
- , —, and C. DeMott, 2005: Simulations of the atmospheric general circulation using a cloud-resolving model as a superparameterization of physical processes. *J. Atmos. Sci.*, **62**, 2136–2154.
- Lee, M.-I., I.-S. Kang, and B. E. Mapes, 2003: Impacts of cumulus convection parameterization on aqua-planet AGCM simulations of tropical intraseasonal variability. *J. Meteor. Soc. Japan*, **81**, 963–992.
- Liebmann, B., H. H. Hendon, and J. D. Glick, 1994: The relationship between tropical cyclones of the western Pacific and Indian Oceans and the Madden-Julian oscillation. *J. Meteor. Soc. Japan*, **72**, 401–411.
- Lin, J.-L., and Coauthors, 2006: Tropical intraseasonal variability in 14 IPCC AR4 climate models. Part I: Convective signals. *J. Climate*, **19**, 2665–2690.
- , M.-I. Lee, D. Kim, I.-S. Kang, and D. M. W. Frierson, 2008: The impacts of convective parameterization and moisture triggering on AGCM-simulated convectively coupled equatorial waves. *J. Climate*, **21**, 883–909.
- Luo, Z., and G. L. Stephens, 2006: An enhanced convection-wind-evaporation feedback in a superparameterization GCM (SP-GCM) depiction of the Asian summer monsoon. *Geophys. Res. Lett.*, **33**, L06707, doi:10.1029/2005GL025060.
- Madden, R. A., and P. R. Julian, 1971: Detection of a 40–50 day oscillation in the zonal wind in the tropical Pacific. *J. Atmos. Sci.*, **28**, 702–708.
- , and —, 1972: Description of global-scale circulation cells in the tropics with a 40–50 day period. *J. Atmos. Sci.*, **29**, 1109–1123.
- Maloney, E. D., and D. L. Hartmann, 2000a: Modulation of eastern North Pacific hurricanes by the Madden–Julian oscillation. *J. Climate*, **13**, 1451–1460.
- , and —, 2000b: Modulation of hurricane activity in the Gulf of Mexico by the Madden-Julian oscillation. *Science*, **287**, 2002–2004.
- , and —, 2001: The sensitivity of intraseasonal variability in the NCAR CCM3 to changes in convective parameterization. *J. Climate*, **14**, 2015–2034.
- , and A. H. Sobel, 2004: Surface fluxes and ocean coupling in the tropical intraseasonal oscillation. *J. Climate*, **17**, 4368–4386.
- , —, and W. M. Hannah, 2010: Intraseasonal variability in an aquaplanet general circulation model. *J. Adv. Model. Earth Syst.*, **2**.
- Moorthi, S., and M. J. Suarez, 1992: Relaxed Arakawa–Schubert: A parameterization of moist convection for general circulation models. *Mon. Wea. Rev.*, **120**, 978–1002.
- Neale, R. B., J. H. Richter, and M. Jochum, 2008: The impact of convection on ENSO: From a delayed oscillator to a series of events. *J. Climate*, **21**, 5904–5924.
- Neelin, J. D., O. Peters, and K. Hales, 2009: The transition to strong convection. *J. Atmos. Sci.*, **66**, 2367–2384.
- Numaguti, A., M. Takahashi, T. Nakajima, and A. Sumi, 1995: Development of an atmospheric general circulation model. *Climate Syst. Dyn. Model.*, **3**, 1–27.
- Peters, O., and J. D. Neelin, 2006: Critical phenomena in atmospheric precipitation. *Nat. Phys.*, **2**, 393–396, doi:10.1038/nphys314.
- Raymond, D. J., 2001: A new model of the Madden–Julian oscillation. *J. Atmos. Sci.*, **58**, 2807–2819.
- Rienecker, M. M., and Coauthors, 2008: The GEOS-5 data assimilation system: Documentation of versions 5.0.1, 5.1.0, and 5.2.0. Technical Report Series on Global Modeling and Data Assimilation, Vol. 27, NASA Tech. Rep. 104606, 101 pp.
- Simmons, A., S. Uppala, D. Dee, and S. Kobayashi, 2007: ERA-Interim: New ECMWF reanalysis products from 1989 onwards. *ECMWF Newsletter*, No. 110, ECMWF, Reading, United Kingdom, 25–35.
- Slingo, J. M., and Coauthors, 1996: Intraseasonal oscillations in 15 atmospheric general circulation models: Results from an AMIP diagnostic subproject. *Climate Dyn.*, **12**, 325–357.
- Sobel, A. H., E. D. Maloney, G. Bellon, and D. M. Frierson, 2010: Surface fluxes and tropical intraseasonal variability: A reassessment. *J. Adv. Model. Earth Syst.*, **2**, 27 pp.
- Sperber, K. R., and H. Annamalai, 2008: Coupled model simulations of boreal summer intraseasonal (30–50 day) variability, Part 1: Systematic errors and caution on use of metrics. *Climate Dyn.*, **31**, 345–372.
- Stan, C., M. Khairoutdinov, C. A. DeMott, V. Krishnamurthy, D. M. Straus, D. A. Randall, J. L. Kinter III, and J. Shukla, 2010: An ocean-atmosphere climate simulation with an embedded cloud resolving model. *Geophys. Res. Lett.*, **37**, L01702, doi:10.1029/2009GL040822.
- Takayabu, Y. N., T. Iguchi, M. Kachi, A. Shibata, and H. Kanzawa, 1999: Abrupt termination of the 1997–98 El Niño in response to a Madden-Julian oscillation. *Nature*, **402**, 279–282.
- Thayer-Calder, K., and D. Randall, 2009: The role of convective moistening in the Madden–Julian oscillation. *J. Atmos. Sci.*, **66**, 3297–3312.
- Tokioka, T., K. Yamazaki, A. Kitoh, and T. Ose, 1988: The equatorial 30–60 day oscillation and the Arakawa–Schubert penetrative cumulus parameterization. *J. Meteor. Soc. Japan*, **66**, 883–901.
- Wang, W. Q., and M. E. Schlesinger, 1999: The dependence on convection parameterization of the tropical intraseasonal oscillation simulated by the UIUC 11-layer atmospheric GCM. *J. Climate*, **12**, 1423–1457.
- Wheeler, M. C., and J. L. McBride, 2005: Australian-Indonesian monsoon. *Intraseasonal Variability in the Atmosphere–Ocean Climate System*, W. K.-M. Lau and D. E. Waliser, Eds., Springer, 125–173.
- Yasunari, T., 1979: Cloudiness fluctuations associated with the Northern Hemisphere summer monsoon. *J. Meteor. Soc. Japan*, **57**, 227–242.
- Zhang, G. J., and N. McFarlane, 1995: Sensitivity of climate simulations to the parameterization of cumulus convection in the Canadian Climate Centre general circulation model. *Atmos.–Ocean*, **33**, 407–446.
- , and M. Mu, 2005: Simulation of the Madden–Julian oscillation in the NCAR CCM3 using a revised Zhang–McFarlane convection parameterization scheme. *J. Climate*, **18**, 4046–4064.
- Zhu, H., H. Hendon, and C. Jakob, 2009: Convection in a parameterized and superparameterized model and its role in the representation of the MJO. *J. Atmos. Sci.*, **66**, 2796–2811.